



ARL-TR-8086 • Aug 2017



US Army Research Laboratory

# Experimental Flight Characterization of a Canard-Controlled, Subsonic Missile

by Frank Fresconi, Ilmars Celmins, James Maley, and  
Bryant Nelson

Approved for public release; distribution is unlimited.

## **NOTICES**

### **Disclaimers**

The findings in this report are not to be construed as an official Department of the Army position unless so designated by other authorized documents.

Citation of manufacturer's or trade names does not constitute an official endorsement or approval of the use thereof.

Destroy this report when it is no longer needed. Do not return it to the originator.



# Experimental Flight Characterization of a Canard-Controlled, Subsonic Missile

by Frank Fresconi, Ilmars Celmins, James Maley, and  
Bryant Nelson

*Weapons and Materials Research Directorate, ARL*

REPORT DOCUMENTATION PAGE				Form Approved OMB No. 0704-0188	
<p>Public reporting burden for this collection of information is estimated to average 1 hour per response, including the time for reviewing instructions, searching existing data sources, gathering and maintaining the data needed, and completing and reviewing the collection information. Send comments regarding this burden estimate or any other aspect of this collection of information, including suggestions for reducing the burden, to Department of Defense, Washington Headquarters Services, Directorate for Information Operations and Reports (0704-0188), 1215 Jefferson Davis Highway, Suite 1204, Arlington, VA 22202-4302. Respondents should be aware that notwithstanding any other provision of law, no person shall be subject to any penalty for failing to comply with a collection of information if it does not display a currently valid OMB control number.</p> <p><b>PLEASE DO NOT RETURN YOUR FORM TO THE ABOVE ADDRESS.</b></p>					
1. REPORT DATE (DD-MM-YYYY) August 2017		2. REPORT TYPE Technical Report		3. DATES COVERED (From - To) July 2016–July 2017	
4. TITLE AND SUBTITLE Experimental Flight Characterization of a Canard-Controlled, Subsonic Missile				5a. CONTRACT NUMBER	
				5b. GRANT NUMBER	
				5c. PROGRAM ELEMENT NUMBER	
6. AUTHOR(S) Frank Fresconi, Ilmars Celmins, James Maley, and Bryant Nelson				5d. PROJECT NUMBER AH80	
				5e. TASK NUMBER	
				5f. WORK UNIT NUMBER	
7. PERFORMING ORGANIZATION NAME(S) AND ADDRESS(ES) US Army Research Laboratory Weapons and Materials Research Directorate (ATTN: RDRL-WML-E) Aberdeen Proving Ground, MD 21005-5066				8. PERFORMING ORGANIZATION REPORT NUMBER  ARL-TR-8086	
9. SPONSORING/MONITORING AGENCY NAME(S) AND ADDRESS(ES)				10. SPONSOR/MONITOR'S ACRONYM(S)	
				11. SPONSOR/MONITOR'S REPORT NUMBER(S)	
12. DISTRIBUTION/AVAILABILITY STATEMENT Approved for public release; distribution is unlimited.					
13. SUPPLEMENTARY NOTES					
14. ABSTRACT <p>The goal of this study is to improve understanding of maneuvering flight and reduce aerodynamic uncertainty of guided munitions to compress the iterative design cycle and realize enhanced maneuverability vehicles. To accomplish this, novel dynamic wind tunnel and spark range flight experiments were performed. An actively controlled vehicle was mounted on a 3 degree-of-freedom gimbal in a wind tunnel with balance, Euler angle, and canard deflection instrumentation. Free-flight spark range firings were conducted with various configurations to isolate control aerodynamics and induce a spectra of angle of attack. An aerodynamic model was postulated to capture high maneuver phenomena such as flow separation and vortex interactions, which were encountered during experiments. This aerodynamic model was used with the experimental data in a parameter estimation algorithm to obtain static and dynamic aerodynamics. Results confirm the novel experimental and aerodynamic modeling approaches and provide validation data for computations.</p>					
15. SUBJECT TERMS subsonic missile, canard control, aerodynamics, spark range, wind tunnel, flight dynamics					
16. SECURITY CLASSIFICATION OF:			17. LIMITATION OF ABSTRACT  UU	18. NUMBER OF PAGES  40	19a. NAME OF RESPONSIBLE PERSON Frank Fresconi
a. REPORT Unclassified	b. ABSTRACT Unclassified	c. THIS PAGE Unclassified			19b. TELEPHONE NUMBER (Include area code) 410-306-0794

## Contents

---

List of Figures	iv
List of Tables	iv
Acknowledgments	v
1. Introduction	1
2. Flight Modeling	3
3. Dynamic Wind Tunnel Experiments	5
4. Spark Range Firings	8
5. Analysis Approach	11
6. Results	13
7. Conclusions	25
8. References	26
List of Symbols, Abbreviations, and Acronyms	29
Distribution List	30

## List of Figures

Fig. 1	Dynamic wind tunnel experimental setup.....	6
Fig. 2	High-speed photography of vehicle undergoing full roll-pitch-yaw motion over 3 distinct flight phases during dynamic wind tunnel experiments.....	7
Fig. 3	Spark range setup.....	10
Fig. 4	High-speed photography from firing of vehicle with deploying fins and canards.....	11
Fig. 5	Onboard sensor data for free motion, open- and closed-loop flight profile for roll-pitch-yaw in dynamic wind tunnel .....	13
Fig. 6	Aerodynamic coefficients from balance measurements in dynamic wind tunnel (left = axial force, right = normal force).....	14
Fig. 7	Free motion pitching in dynamic wind tunnel .....	15
Fig. 8	Open-loop control pitching in dynamic wind tunnel (left = pitch angle, right = deflections).....	16
Fig. 9	In-plane static moment coefficients from parameter estimation in dynamic wind tunnel (left = body-fins, right = canard).....	16
Fig. 10	Summary linear in-plane static moment coefficients in dynamic wind tunnel.....	17
Fig. 11	Free motion rolling in dynamic wind tunnel.....	18
Fig. 12	Spark shadowgraphs (left = vertical, right = horizontal) .....	18
Fig. 13	Flight motion in spark range (top left = roll, top right = pitch and yaw, bottom = center of gravity) .....	19
Fig. 14	Resonance behavior of vehicle in spark range.....	20
Fig. 15	Total angle of attack for all spark range flights .....	21
Fig. 16	Zero-yaw axial force coefficient.....	22
Fig. 17	Linear normal force coefficient .....	23
Fig. 18	Linear in-plane static moment coefficient .....	24
Fig. 19	Damping coefficients (left = pitch, right = roll) .....	24

## List of Tables

Table 1	Spark range flight vehicles with mass properties .....	9
---------	--	---

## Acknowledgments

---

The authors appreciate the contributions of Bernard Guidos (US Army Research Laboratory [ARL]), the crew of the Transonic Experimental Facility, John Heath (ARL), Barry Hudler (ARL), Ken Willan (ARL), Eric Miller (ARL), Bill Aubry (ARL), and Jarid Kranz (ARL). Also, Bobby Hall (ARL) and the machinists at the Weapons and Materials Research Directorate machine shop, Ron Anderson (ARL), Joe Colburn (ARL), Dan Weber (Edgewood Chemical Biological Center [ECBC]), and the crew of engineers and technicians at the ECBC wind tunnels.

INTENTIONALLY LEFT BLANK.

# 1. Introduction

---

The motivation for this study is to enhance control authority and overall system performance by better understanding the maneuvering flight response of canard-controlled, subsonic missiles. High-maneuverability flight features complex and often related mechanisms including separation, vortex interactions, and unsteady flows. Flows over 2-D airfoils have been studied extensively and show that separation occurs at the trailing edge due to adverse pressure gradients at appreciable angle of attack.<sup>1</sup> The basic flow mechanisms are different for slender bodies of revolution at angle of attack.<sup>2</sup> Symmetric vortices are shed from the leeward side at lower angle of attack. As angle of attack increases the vortices become asymmetric and periodic, which results in side forces and moments. Vortices shed off the slender body impinge on aft-mounted fins, which alters the pressure distribution and associated loading in a complex manner.<sup>3</sup> Another flow mechanism related to canard-controlled missiles is a simple fin downstream of another fin.<sup>4,5</sup> Vortices shed off the upstream deflected fin and turn the flow over the downstream fin. This interaction effectively induces an angle of attack in the downstream fin.

These canonical mechanisms are known but extension to canard-controlled missiles with time-dependent, 3-D effects between closely spaced slender bodies, stabilizing fins, and deflecting canards over a wide range of aerodynamic angles and angular rates is poorly understood. Many studies of canard-controlled missile configurations focus on the relationship between aerodynamic coefficients and the vehicle outer mold line for different independent parameters (e.g., total angle of attack, aerodynamic roll angle).<sup>6-9</sup> Investigations into problems maintaining roll control due to adverse canard vortex fin interactions have been conducted.<sup>10-12</sup>

A fundamental understanding of flight behaviors for subsonic, canard-controlled missiles is lacking and important to weapons designers. Reduction in lift due to separation on the canards largely dictates the maximum trim angle of the vehicle and subsequent maneuverability. The induced downwash on fins from deflected canards reduces stability and can yield unsatisfactory flight performance if not properly modeled.<sup>13-15</sup> Solving these scientific problems is challenging due to the complex physical mechanisms and large parameter space (e.g., fin, canard, ogive geometry, and dependencies on aerodynamic angles and angular rates). The knowledge gained enables vehicle optimization subject to mission objectives and constraints.

This study contributes to the state of the art by extending experimental flight characterization techniques for maneuvering munitions in well-controlled

environments, accurately quantifying aerodynamics for a specific vehicle, and formulating general aerodynamic models for maneuvering munitions. Aerodynamic models capture the complex fluid mechanics related to atmospheric vehicles in mathematical form.<sup>16,17</sup> Aerodynamic modeling for configurations containing control surfaces and severe nonlinearities in angle of attack often resorts to table lookups. This study proposes more equation-based aerodynamic models representing complicated phenomena such as canard deflections, separation, and vortex interactions. The approach in this study improves physical insight and is easily incorporated into model-based flight control design.

Semiempirical aerodynamic and computational fluid dynamics (CFD) predictions for munitions have advanced tremendously.<sup>18–20</sup> The uncertainty associated with extending these techniques to novel vehicle configurations—especially when separation, vortex interactions, and unsteadiness may be present—requires validation. This report provides experimental results on a subsonic, canard-controlled vehicle approximately 5 cal. long. The information provided in this report is also critical because accurate flight characterization underpins flight simulation and development of sensor, algorithm, embedded processing, and control actuation technologies.

Dynamic wind tunnel and spark range free-flight experimental techniques are advanced in this study. Both techniques offer a well-controlled environment for investigating flight behavior. Dynamic wind tunnel experiments typically mount the model in the tunnel with certain degrees of freedom available. Models may be released from nonequilibrium points or driven via motors fixed to the model or internally actuated control surfaces to induce flight motion. Measurements usually consist of vehicle motion (e.g., Euler angles from potentiometers, angular rates from gyroscopes). Most studies emphasize aircraft flight characteristics.<sup>21</sup> Dynamic wind tunnel investigations on munitions historically focus on planar pitching motions to deduce pitch damping moments.<sup>22</sup> More recently, the roll-<sup>23</sup> and pitch-channel<sup>24</sup> flight behavior was examined for canard-controlled, subsonic missiles equipped with onboard sensing, processing, and actuation. This study extends dynamic wind tunnel techniques for maneuvering munitions by considering full roll-pitch-yaw motion and incorporating balance measurements in a limited-intrusive manner.

The spark range technique is often considered the gold standard in experimental aerodynamics since the model is in free-flight, the enclosure has well-known atmospheric conditions (e.g., no wind), and the time-stamped measurements of center-of-gravity and Euler angles are highly accurate.<sup>25</sup> In contrast, wind tunnels suffer from flow quality issues along with sting and wall effects.

This report demonstrates advanced spark range experimental techniques by flying vehicles with different configurations (e.g., body-fins, body-fins-canards) to isolate control aerodynamics. In addition, spark range experiments were designed using a persistent excitation approach (i.e., roll-yaw resonance with asymmetric mass) to improve data quality.<sup>26</sup>

The report presents the flight models including the aerodynamic model for rigid and moveable aerodynamic surfaces, vehicle kinematics and dynamics, and actuator dynamics. Next, the dynamic wind tunnel experiments and spark range firings are discussed. A description is given of the experimental data analysis techniques. Results are provided followed by summary findings in the conclusion.

## 2. Flight Modeling

---

The aerodynamic model expresses the functional dependency of the aerodynamic forces and moments for this specific vehicle class. Static and dynamic (rate dependent) aerodynamic behavior with nonlinearities in angle of attack and Mach number are considered. Variation with aerodynamic roll angle, damping forces, and unsteadiness is neglected. Angle-of-attack nonlinearities are modeled using polynomials. Piecewise polynomials are applied to capture sharp nonlinearities due to flow separation on canards. This study treats the rigid (i.e., body-fins) and moveable (canards) aerodynamic surfaces separately. The vehicle diameter was used as the reference length and the moment reference center was 3.19 cal. from the nose for lateral aerodynamic moments in this study.

The aerodynamic model for the rigid aerodynamic surfaces is given in Eqs. 1–6. The static in-plane forces feature trims and terms that vary linearly and nonlinearly with angle of attack (angle of attack is used broadly throughout this technical report to describe total angle of attack, angle of sideslip, or angle of attack). A linear static out-of-plane force is included. The aerodynamic moments consider in-plane static (trim, linear, nonlinear), out-of-plane static (linear), damping, and flow interaction terms. The flow interaction consists of an aerodynamic coefficient and scaling with control deflection magnitude. This modeling approach captures adverse roll control<sup>10–12</sup> (i.e., reduction in control roll moment due to vortices shed off canards impinging on fins) and reduction in pitch-yaw stability<sup>13–15</sup> (i.e., induced downwash on fins from canards).

$$X = -QS \left( C_{X_0} + C_{X_{\bar{\alpha}^2}} \sin^2 \bar{\alpha} + C_{X_{\bar{\alpha}^4}} \sin^4 \bar{\alpha} \right), \quad (1)$$

$$Y = -QS \left( C_{Y_0} + C_{N_\alpha} \sin \beta + C_{N_{\alpha^3}} \sin^3 \beta + C_{N_{\alpha^5}} \sin^5 \beta - C_{Y_\alpha} \sin \alpha \right), \quad (2)$$

$$Z = -QS \left( C_{Z_0} + C_{N_\alpha} \sin \alpha + C_{N_{\alpha^3}} \sin^3 \alpha + C_{N_{\alpha^5}} \sin^5 \alpha + C_{Y_\alpha} \sin \beta \right), \quad (3)$$

$$L = QSD \left( C_{l_0} + C_{l_p} \frac{pD}{2V} + C_{l_{\delta_p}} \sin \delta_p \right), \quad (4)$$

$$M = QSD \left( C_{m_0} + C_{m_\alpha} \sin \alpha + C_{m_{\alpha^3}} \sin^3 \alpha + C_{m_{\alpha^5}} \sin^5 \alpha + C_{m_q} \frac{qD}{2V} + C_{n_\alpha} \sin \beta + C_{m_{\delta_q}} \sin \delta_q \right), \quad (5)$$

and

$$N = QSD \left( -C_{n_0} - C_{m_\alpha} \sin \beta - C_{m_{\alpha^3}} \sin^3 \beta - C_{m_{\alpha^5}} \sin^5 \beta + C_{m_q} \frac{rD}{2V} + C_{n_\alpha} \sin \alpha + C_{m_{\delta_q}} \sin \delta_r \right). \quad (6)$$

The aerodynamic model for moveable aerodynamic surfaces are shown in Eqs. 7–12. The forces and moments are summed over  $i$  surfaces arrayed around the body at specific roll angles. Static in-plane forces and moments include trims and linear and nonlinear dependencies with local angle of attack. Piecewise polynomials, with different coefficients over different angle of attack regions, are applied to model extreme nonlinearities due to changes in flow state (i.e., separation). Out-of-plane forces and moments on the moveable aerodynamic surfaces are neglected.

$$\hat{X} = \sum_{i=1}^{N_m} -Q_i S \left( \hat{C}_{X_0} + \hat{C}_{X_{\bar{\alpha}^2}} \sin^2 \bar{\alpha}_i + \hat{C}_{X_{\bar{\alpha}^4}} \sin^4 \bar{\alpha}_i \right), \quad (7)$$

$$\hat{Y} = \sum_{i=1}^{N_m} -Q_i S \left( \hat{C}_{Z_0} + \hat{C}_{N_\alpha} \sin \alpha_i + \hat{C}_{N_{\alpha^3}} \sin^3 \alpha_i + \hat{C}_{N_{\alpha^5}} \sin^5 \alpha_i \right) (-\sin \phi_i), \quad (8)$$

$$\hat{Z} = \sum_{i=1}^{N_m} -Q_i S \left( \hat{C}_{Z_0} + \hat{C}_{N_\alpha} \sin \alpha_i + \hat{C}_{N_{\alpha^3}} \sin^3 \alpha_i + \hat{C}_{N_{\alpha^5}} \sin^5 \alpha_i \right) \cos \phi_i, \quad (9)$$

$$\hat{L} = \sum_{i=1}^{N_m} Q_i SD \left( \hat{C}_{l_0} + \hat{C}_{l_{\bar{\alpha}}} \sin \bar{\alpha}_i + \hat{C}_{l_{\bar{\alpha}^3}} \sin^3 \bar{\alpha}_i + \hat{C}_{l_{\bar{\alpha}^5}} \sin^5 \bar{\alpha}_i \right), \quad (10)$$

$$\hat{M} = \sum_{i=1}^{N_m} Q_i SD \left( \hat{C}_{m_0} + \hat{C}_{m_\alpha} \sin \alpha_i + \hat{C}_{m_{\alpha^3}} \sin^3 \alpha_i + \hat{C}_{m_{\alpha^5}} \sin^5 \alpha_i \right) \cos \phi_i, \quad (11)$$

and

$$\hat{N} = \sum_{i=1}^{N_m} Q_i SD \left( \hat{C}_{m_0} + \hat{C}_{m_\alpha} \sin \alpha_i + \hat{C}_{m_{\alpha^3}} \sin^3 \alpha_i + \hat{C}_{m_{\alpha^5}} \sin^5 \alpha_i \right) \sin \phi_i. \quad (12)$$

The relationship between the velocities of 2 fixed points (i.e., vehicle center-of-gravity and moveable aerodynamic surface center-of-pressure) on a rigid body is given in Eqs. 13–15. This method for calculating the wind vector at each control surface implicitly captures aerodynamic damping through the cross-product term. This wind vector is used to calculate the angle of attack at each control surface and subsequent aerodynamic forces and moments.

$$u_i = u - r d_y + q d_z, \quad (13)$$

$$v_i = \cos \phi_i (v + r d_x - p d_z) + \sin \phi_i (w - q d_x + p d_y), \quad (14)$$

and

$$w_i = -\sin \phi_i (v + r d_x - p d_z) + \cos \phi_i (w - q d_x + p d_y). \quad (15)$$

The equations governing the flight motion of atmospheric vehicles can be found in the literature<sup>16,26</sup> and are given next. The rigid body kinematics (Eqs. 16 and 17) and dynamics (Eqs. 18 and 19) are obtained straightforwardly from considering

first principles. The rotational dynamics expressions used in this study (Eq. 19) feature a full moment of inertia tensor due to the inclusion of asymmetric mass configurations in experiments.

$$\begin{bmatrix} \dot{x} \\ \dot{y} \\ \dot{z} \end{bmatrix} = \begin{bmatrix} c_\theta c_\psi & s_\phi s_\theta c_\psi - c_\phi s_\psi & c_\phi s_\theta c_\psi + s_\phi s_\psi \\ c_\theta s_\psi & s_\phi s_\theta s_\psi + c_\phi c_\psi & c_\phi s_\theta s_\psi + s_\phi c_\psi \\ -s_\theta & s_\phi c_\theta & c_\phi c_\theta \end{bmatrix} \begin{bmatrix} u \\ v \\ w \end{bmatrix}, \quad (16)$$

$$\begin{bmatrix} \dot{\phi} \\ \dot{\theta} \\ \dot{\psi} \end{bmatrix} = \begin{bmatrix} 1 & s_\phi t_\theta & c_\phi t_\theta \\ 0 & c_\phi & -s_\phi \\ 0 & s_\phi/c_\theta & c_\phi/c_\theta \end{bmatrix} \begin{bmatrix} p \\ q \\ r \end{bmatrix}, \quad (17)$$

$$\begin{bmatrix} \dot{u} \\ \dot{v} \\ \dot{w} \end{bmatrix} = \frac{1}{m} \begin{bmatrix} X + \hat{X} - g s_\theta \\ Y + \hat{Y} + g s_\phi c_\theta \\ Z + \hat{Z} + g c_\phi c_\theta \end{bmatrix} - \begin{bmatrix} 0 & -r & q \\ r & 0 & -p \\ -q & p & 0 \end{bmatrix} \begin{bmatrix} u \\ v \\ w \end{bmatrix}, \quad (18)$$

and

$$\begin{bmatrix} \ddot{p} \\ \ddot{q} \\ \ddot{r} \end{bmatrix} = \begin{bmatrix} I_{XX} & I_{XY} & I_{XZ} \\ I_{XY} & I_{YY} & I_{YZ} \\ I_{XZ} & I_{YZ} & I_{ZZ} \end{bmatrix}^{-1} \begin{bmatrix} L + \hat{L} \\ M + \hat{M} \\ N + \hat{N} \end{bmatrix} - \begin{bmatrix} I_{XX} & I_{XY} & I_{XZ} \\ I_{XY} & I_{YY} & I_{YZ} \\ I_{XZ} & I_{YZ} & I_{ZZ} \end{bmatrix}^{-1} \begin{bmatrix} 0 & -r & q \\ r & 0 & -p \\ -q & p & 0 \end{bmatrix} \begin{bmatrix} I_{XX} & I_{XY} & I_{XZ} \\ I_{XY} & I_{YY} & I_{YZ} \\ I_{XZ} & I_{YZ} & I_{ZZ} \end{bmatrix} \begin{bmatrix} p \\ q \\ r \end{bmatrix}. \quad (19)$$

The actuator dynamics driving the motion of each canard were modeled using a second-order response with time delay.

$$\ddot{\delta}(t) + 2\xi\omega\dot{\delta}(t) + \omega^2\delta(t) = \delta_c(t - t_D). \quad (20)$$

### 3. Dynamic Wind Tunnel Experiments

These flight models were applied to observations taken during a series of dynamic wind tunnel experiments. The materials for the dynamic wind tunnel experiments consisted of a model, sting, balance and wind tunnel. Two wind tunnels at the US Army's Edgewood Chemical and Biological Center were used. One was a continuous flow, in-draft wind tunnel that was operated at a Mach number of approximately 0.2 in a test section of 0.76 m wide  $\times$  0.61 m high. An internal strain gage balance with a 0.0095-m diameter and 5-axis capability (no roll moment) obtained the aerodynamic loads in this tunnel. The balance was fixtured to a high-strength steel sting that suspended the model in the test section. The other tunnel was an intermittent flow blow-down tunnel. This tunnel was operated at a Mach number of approximately 0.6 in a test section of 0.51 m wide  $\times$  0.51 m high. Both tunnels were utilized to meet experimental needs in Mach number and instrumentation.

The model included a vehicle equipped with 10 fins and 4 independently actuated canards, a release mechanism, gimbals, onboard sensors, processing, data storage,

wireless data transmitter, and power.<sup>27</sup> A digital signal processor (DSP) hosted real-time flight control algorithms and packaged data to onboard storage and a transmitter in the S band. A gimbal mechanism was designed that permitted 3 degree-of-freedom motion of the model with respect to the sting. This mechanism featured a locking mechanism to isolate motion in the roll, pitch, or yaw directions. Encoders were mounted to the gimbal assembly and the signals passed through an analog-to-digital converter prior to being sampled by the DSP to measure the angular motion. The model was instrumented with triaxial angular rate sensors and accelerometers. Servomechanisms drove 4 canards based on flight control commands from the DSP. Potentiometers measuring the canard deflections angles were incorporated into the onboard data-stream. A mechanical fixture installed between the rear of the model and the sting enabled the model to be released from a nonequilibrium point (i.e., angle of attack) by pulling a string at the beginning of each run. The model was 0.083 m in diameter, 0.425 m long with the gimbal rotation point 0.263 m from the nose; weighed 3.141 kg and had axial and transverse moments-of-inertia of 0.00379 and 0.039948 kg-m<sup>2</sup>, respectively. Fixing the location of a translatable internal mass allowed the center of gravity to match the gimbal pivot point. The model mounted in the tunnel is shown in Fig. 1.

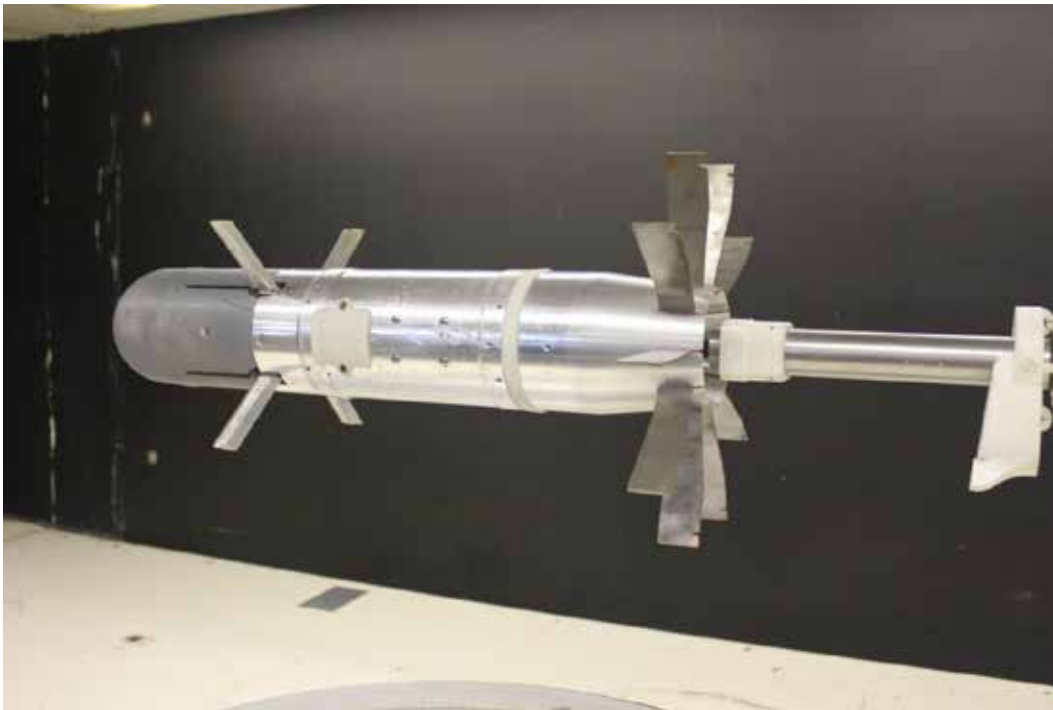


**Fig. 1     Dynamic wind tunnel experimental setup**

Dynamic wind tunnel experiments proceeded in the following manner. First, the embedded processor was loaded with the appropriate software and the model was

assembled and mounted on the sting in the tunnel. The battery was activated and the model release mechanism was configured. The tunnel was turned on. Once steady-state flow was achieved the model release mechanism was removed, the model performed the flight maneuvers dictated by the software, and onboard sensor, balance data, and high-speed video were collected.

Each wind tunnel run typically consisted of 3 distinct phases: free motion of the vehicle from a nonequilibrium point with no canard deflections, open-loop control canard deflections, and closed-loop control canard deflections. Experiments were performed with full 3 degree-of-freedom motion and with motion constrained only in the roll and pitch axes, respectively, to isolate flight behaviors. Figure 2 provides a representative dynamic wind tunnel high-speed photography data set.



**Fig. 2 High-speed photography of vehicle undergoing full roll-pitch-yaw motion over 3 distinct flight phases during dynamic wind tunnel experiments**

Integration of multidisciplinary technologies in a small (0.083 m diameter) form factor was a major technical challenge overcome in these dynamic wind tunnel experiments. Instrumenting experiments with simultaneous onboard sensor and balance data acquisition in such a manner that the rig featured minimal intrusion (i.e., balance mounted to sting running through model base to 3 degree-of-freedom gimbal with low friction bearings) while accommodating appreciable angular motion ( $\sim \pm 8^\circ$ ) was another significant technical achievement and represents the first such example recorded in the literature.

## 4. Spark Range Firings

---

In addition to wind tunnel experiments, spark range firings were also conducted to better assess the free-flight aerodynamics. The spark range at the US Army Research Laboratory's Transonic Experimental Facility features 25 measurement stations in a darkened, enclosed building over 250 m long. Each station is equipped with a light screen, delay unit, spark source, surveyed fiducials, and 2 orthogonal cameras for capturing shadowgraphs. As the vehicle flies past each station the light screen triggers, which sets off the high-intensity, short-duration spark source after the appropriate delay to obtain the orthogonal shadowgraphs. Postprocessing of the shadowgraphs and trigger times yields the center-of-gravity location and Euler angles, which, along with meteorological data, are used to obtain aerodynamic coefficients in a parameter estimation algorithm.

Six vehicles were flown through the spark range with different internal and external configurations. Two external configurations were considered—body-fins and body-fins-canards—to isolate the control (i.e., canard) aerodynamics. Two internal configurations—symmetric and asymmetric—were built to fly the vehicles over a wider range of total angle of attack. Vehicles with internal asymmetry featured a tungsten mass off of the longitudinal axis of symmetry. This configuration yielded a trim angle in the flight, which resulted in higher total angle of attack (especially when the vehicles flew through roll-yaw resonance).<sup>26</sup> Cant was added to some of the vehicles to induce roll rate. A summary of the vehicles flown through the spark range along with mass properties are collated in Table 1. The mass properties were obtained using a combination of precision measurement devices and solid modeling.

**Table 1 Spark range flight vehicles with mass properties**

<b>No. Flights</b>	<b>External configuration</b>	<b>Mass (kg)</b>	<b>Longitudinal center-of- gravity (m from nose)</b>	<b>Lateral center-of- gravity (m from nose)</b>	<b>Axial inertia (kg-m<sup>2</sup>)</b>	<b>Trans. inertia (kg-m<sup>2</sup>)</b>	<b>Cross-axis inertia (kg-m<sup>2</sup>)</b>
1	fin-body with cant	2.595	0.268	0	0.0035614	0.038102	0
1	canard-fin-body with cant	2.499	0.269	0	0.0032600	0.032395	0
1	fin-body without cant	2.595	0.268	0	0.0035614	0.038102	0
1	fin-body without cant	2.792	0.270	0.001	0.0036510	0.038581	0.0002
2	canard-fin-body with cant	2.705	0.272	0.001	0.0033710	0.032891	0.0002

A 0.083-m diameter smoothbore recoilless gun launched the vehicles. Contrary to conventional guns, recoilless guns allow propellant to escape from the rear (i.e., through breech). A heavy counter-mass (~10 times the mass of the projectile exiting the muzzle) was placed in the chamber that traveled toward the open breech (opposite the direction of the projectile) during propellant combustion and controlled the release of gas from the rear. A sand-filled box was placed about 2 m behind the breech to catch the counter-mass. A Frankfort mount was used to place the gun between stations 5 and 6 in the spark range building. The propelling charge was contained within a plastic additive manufacturing housing and used 83 g of M38 propellant with about 2 g of black powder wrapped around an electric match. A shot-start link was used in the vehicle/counter-mass assembly to improve muzzle velocity repeatability. The shot-start link sat in the propulsion chamber and consisted of a small diameter aluminum cylinder with a stress concentration feature. One end of the cylinder was threaded into the rear of the vehicle and the other end of the cylinder was threaded into the front face of the counter-mass. As gas pressure built during the propellant combustion process the shot-start link kept the vehicle and counter-mass from separating and running away until reaching a threshold pressure dictated by failure of the stress concentration feature. These conditions resulted in launch speeds around 225 m/s (~Mach 0.66). The gun setup in the spark range is shown in Fig. 3.



**Fig. 3 Spark range setup**

A series of preliminary firings were conducted with high-speed photography (fixed and flight follower using a rotating mirror), radar, yaw cards, and gun pressure gauges to establish the charge, verify structural integrity, assess flight stability, and validate the flight path prior to spark range firings. These firings were especially critical since the vehicles must fly through an approximately  $2\text{ m} \times 2\text{ m}$  window at each station in the spark range. A representative high-speed photography dataset on a body-fins-canards configuration is provided in Fig. 4.



**Fig. 4 High-speed photography from firing of vehicle with deploying fins and canards**

Significant technical barriers were overcome to obtain accurate aerodynamics of this vehicle in the spark range. The subsonic flight regime, 0.083 m vehicle scale, and inherent maneuverability of the body-fins-canards configuration combine to make flying the vehicles through the instrumentation windows in the spark range a challenge. Gravity drop is significant due to the vehicle speed and ballistic coefficient. The body-fins-canards configuration has a low static margin that increases lateral deviation of the flight off the gun boresight (i.e., aerodynamic jump).<sup>28</sup> Gravity drop and aerodynamic jump considerations forced the gun to be placed within the spark range enclosure.

## 5. Analysis Approach

---

Raw wind tunnel strain gage balance data were converted to aerodynamic coefficients through low-pass filtering, applying calibration (scale factor, cross-axis sensitivities), and atmospheric (density, sound speed) and flow speed measurements. These coefficients were combined with the aerodynamic angles

obtained from the encoders in a least-squares regression analysis to yield the aerodynamics. The axial force and normal force were the focus of the balance data analysis since vehicle translation was constrained during dynamic wind tunnel experiments. The moments were unconstrained by the gimbal mechanism (i.e., moment measurements near zero since rotational dynamics always achieving equilibrium point); therefore, parameter estimation algorithms were applied to quantify aerodynamic moments.

The maximum likelihood method<sup>29–31</sup> was implemented to determine aerodynamic moments from dynamic wind tunnel and all aerodynamics from spark range firings. This is a nonlinear least-squares technique that seeks to find parameters that minimize a logarithmic function containing the residual between the experimental measurements and the model calculations. The estimated parameters were somewhat different between the dynamic wind tunnel and spark range experiments. The parameter vector for dynamic wind tunnel experiments included the following initial conditions and aerodynamic coefficients for the rigid and moveable surfaces. Actuator dynamics parameters were estimated from these data but these results are outside the scope of this technical report.

$$\Theta = \begin{bmatrix} C_{m_0} & C_{n_0} & C_{m_\alpha} & C_{m_{\alpha^3}} & C_{m_{\delta q}} & C_{m_q} & \hat{C}_{m_0} & \hat{C}_{m_\alpha} & C_{l_0} & C_{l_p} & C_{l_{\delta p}} & \dots \\ \hat{C}_{l_0} & \hat{C}_{l_{\bar{\alpha}}} & \phi_0 & \theta_0 & \psi_0 & p_0 & q_0 & r_0 & & & & \end{bmatrix}. \quad (21)$$

The parameter vector for the spark range problem contained the aerodynamic coefficients and initial conditions shown in Eq. 22.

$$\Theta = \begin{bmatrix} C_{X_0} & C_{X_{\bar{\alpha}^2}} & C_{Y_0} & C_{Z_0} & C_{N_\alpha} & C_{N_{\alpha^3}} & C_{m_0} & C_{n_0} & C_{m_\alpha} & C_{m_{\alpha^3}} & C_{m_{\delta q}} & C_{m_q} & C_{n_\alpha} & \dots \\ C_{l_0} & C_{l_p} & C_{l_{\delta p}} & \hat{C}_{X_0} & \hat{C}_{Z_0} & \hat{C}_{N_\alpha} & \hat{C}_{m_0} & \hat{C}_{m_\alpha} & \hat{C}_{l_0} & \hat{C}_{l_{\bar{\alpha}}} & \dots & & & \\ x_0 & y_0 & z_0 & \phi_0 & \theta_0 & \psi_0 & u_0 & v_0 & w_0 & p_0 & q_0 & r_0 & & \end{bmatrix}. \quad (22)$$

Initial guesses for the parameters in Eqs. 21 and 22 were used to integrate both the nonlinear flight model (Eqs. 1–20) and differential equations for a Jacobian ( $\frac{\partial \mathbf{x}_c}{\partial \Theta}$ ) to the end of the time series. A Newton-Raphson routine was applied to optimize the likelihood function at times containing experimental data. The following equation was used in this method to update the values in the parameter vector. The Levenberg-Marquardt parameter was included to improve conditioning of the Fisher information matrix for some data sets.

$$\Delta \Theta = \left( \sum_{i=1}^{N_M} \frac{\partial \mathbf{x}_{c,i}}{\partial \Theta}^T \mathbb{R}^{-1} \frac{\partial \mathbf{x}_{c,i}}{\partial \Theta} + \xi I \right)^{-1} \sum_{i=1}^{N_M} \frac{\partial \mathbf{x}_{c,i}}{\partial \Theta}^T \mathbb{R}^{-1} \epsilon_i. \quad (23)$$

This procedure was iterated with the adjusted parameters until convergence was achieved.

## 6. Results

A typical dynamic wind tunnel flight profile for roll-pitch-yaw motion is provided in Fig. 5. The Euler angles are contained in the upper plot (roll angle scaled by 0.1 to improve visualization of all data) and angular rates are shown in the middle plot. The lower plot depicts the commanded and achieved canard deflections (different colors correspond to the different canards). The model was released from a  $7^\circ$  pitch angle with zero yaw and roll angle. The free motion phase occurs for the first 2 s and is characterized by no canard deflections. Oscillation and damping of the pitch angle is evident during this phase. The roll angle changes by about  $20^\circ$  and the yaw angle oscillates slightly possibly due to experimental imperfections.

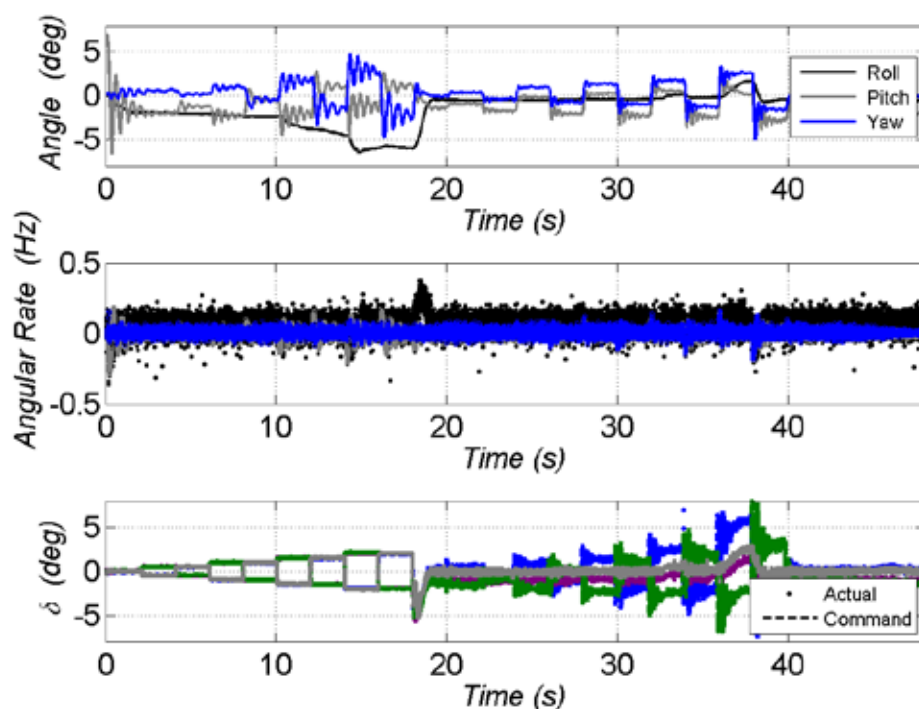


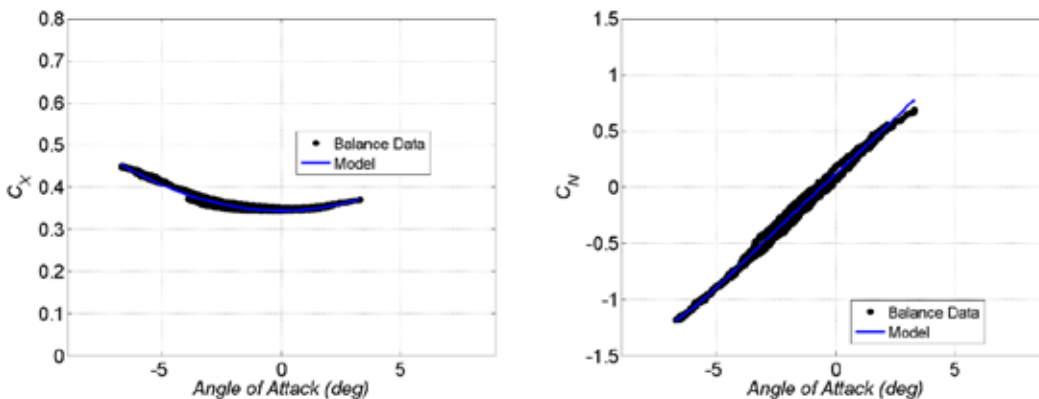
**Fig. 5** Onboard sensor data for free motion, open- and closed-loop flight profile for roll-pitch-yaw in dynamic wind tunnel

The open-loop control phase took place during the next 16 s. Canard commands of opposite sign were gradually increased to  $2^\circ$  in  $0.5^\circ$  increments every 2 s. For example, at 2 s canards were deflected to  $\pm 0.5^\circ$ . Due to the sign convention 2 canards were deflected to positive angles and 2 canards were deflected to negative angles so that the net result caused the body angle of attack to increase. At 4 s the deflection command magnitude stayed the same but the sign changed, which yielded a negative body angle of attack. Deflection command increased to  $1^\circ$  at 6 s

and again switched sign (positive body angle of attack). This cycle of stepping up the deflection command and changing the sign at each deflection command repeated 4 times. The pitch and yaw angles increased and oscillated more as deflection command increased. The roll angle changed during open-loop control potentially due to asynchrony in the deflections or coupling with the lateral dynamics.

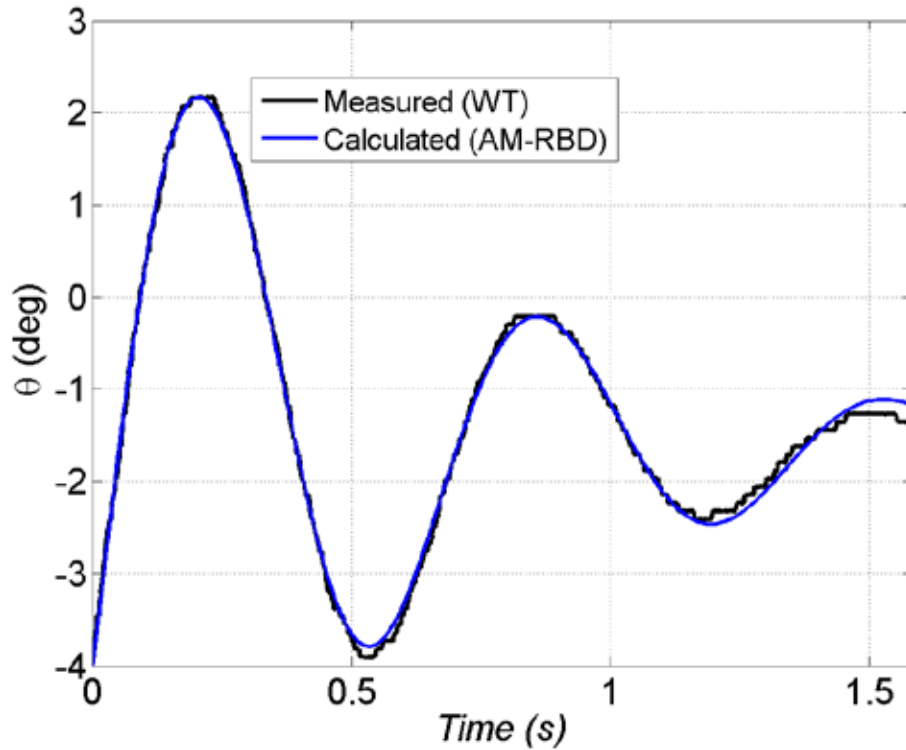
Closed-loop control was performed for the remainder of the run. The control objective was to regulate roll angle and roll, pitch, and yaw angular rates to zero while achieving desired body pitch and yaw angles. The performance of the flight controller is evident in the data. The roll angle is nearly zero within less than 1 s from the start of this phase. Improved damping is illustrated by comparing the closed- and open-loop oscillation in the pitch and yaw angles. The set-point pitch and yaw angles were achieved. The canard deflections commanded by the controller that produced these flight motions is shown in the bottom plot from 16 s onward. Canard stall, and the subsequent reduction in aerodynamic control, were encountered around 37 s. The vehicle was at a high enough angle of attack that the flow separated on one of the canards, which resulted in a loss of control as seen in the increase in the roll angle in the top plot around 37–38 s. Control was recovered in the next set-point as the angle of attack decreased.

Figure 6 provides the balance data obtained during the free motion phase of the dynamic wind tunnel experiments. The least-squares regression for the aerodynamic model is also included in these plots. The axial force coefficient has a minimum of approximately 0.35 at 0° angle of attack. The even-order polynomial captures the increase in axial force with angle of attack. The static normal force coefficient is primarily linear over the angle of attack investigated in these experiments. There is a small trim in the normal force data due to model or tunnel asymmetries.



**Fig. 6 Aerodynamic coefficients from balance measurements in dynamic wind tunnel (left = axial force, right = normal force)**

Measurements of the angular motion in the wind tunnel and parameter estimation calculations using the aerodynamic model and rigid body dynamics are shown in Fig. 7. These data were obtained during the free motion phase with motion constrained to the pitch plane at Mach number 0.17. The root-sum-square error between measurement and calculation was  $0.08^\circ$ , which is on the order of the encoder resolution. These results suggest that the aerodynamic model captures the relevant physical phenomena. The in-plane static moment drives the oscillation frequency. The aerodynamic damping dictates the amplitude decay. The gimbal bearing friction was accounted for by quantifying during laboratory experiments.



**Fig. 7 Free motion pitching in dynamic wind tunnel**

Open-loop control maneuvers with motion constrained to the pitch plane at Mach number 0.57 is provided in Fig. 8. The canard deflections were commanded to  $2^\circ$ , which caused the vehicle to trim around  $3^\circ$  angle of attack. The pitch oscillation frequency and amplitude provide information regarding canard deflection dependencies in the aerodynamics as investigated by Sifton and Fresconi<sup>13</sup> and Sahu and Fresconi.<sup>14</sup> The flow interaction terms were  $C_{l_{\delta_p}} = -2.10$  and  $C_{m_{\delta_q}} = 2.62$ . The root-sum-square error in the pitch angle was  $0.15^\circ$  despite challenges in instrumentation (deflection of canard 2 not measured) and

accommodating experimental practicalities in the analysis (non-ideal response of canard 3, bias in canard 1).

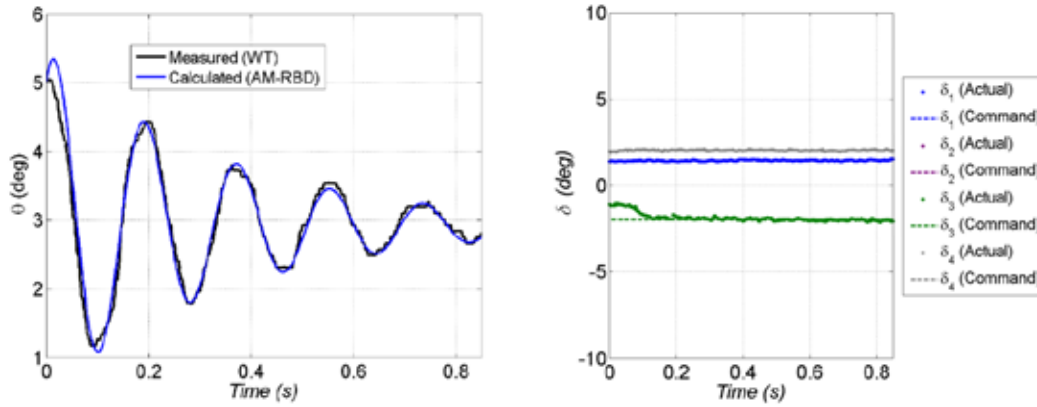


**Fig. 8 Open-loop control pitching in dynamic wind tunnel (left = pitch angle, right = deflections)**

Multiple dynamic wind tunnel experiments over a variety of conditions permits a wider assessment of the flight behavior. In-plane static moment coefficients from numerous experiments are given in Fig. 9. The left-most plot is a function of vehicle angle of attack and has a negative slope since it represents the body-fins contribution (stabilizing). These data are mainly linear over the angle of attack range in the experiments. There is a noticeable trim in the low speed tunnel ( $\sim$ Mach 0.2) potentially due to the sting configuration. The plot on the left is a function of local angle of attack at each canard (Eqs. 13–15) and features a positive slope since it represents the canard contribution (destabilizing). Experiments with canard deflection did not experience small local angle of attack as seen in the gaps around  $0^\circ$  angle of attack in the right plot of Fig. 8.

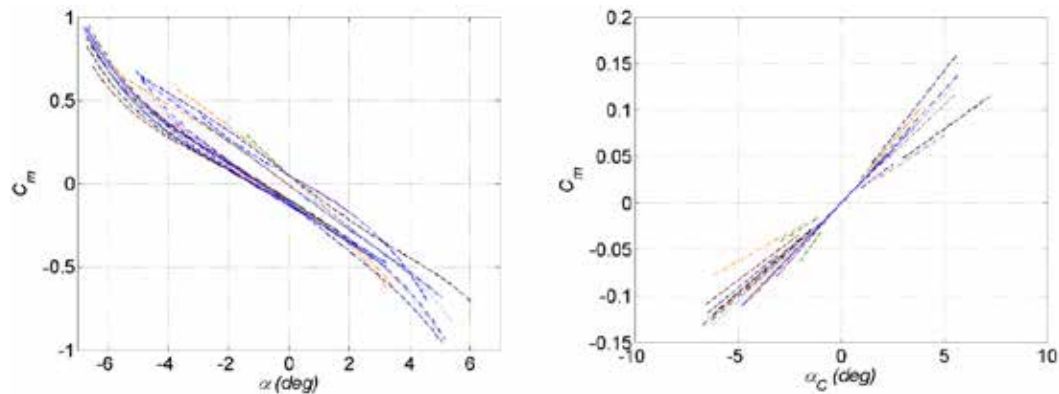


**Fig. 9 In-plane static moment coefficients from parameter estimation in dynamic wind tunnel (left = body-fins, right = canard)**

The in-plane static moment slopes broken out by body-fins and canard components at both Mach numbers from all dynamic wind tunnel runs are shown in Fig. 10. One standard deviation uncertainties, plotted as “X” around the mean data, were higher for the higher Mach number experiments due to rig vibration. The body-fins and canard in-plane static moments are within the uncertainty bounds and consistent across Mach number. Analytically combining the body-fins and canard data to yield the body-fins-canards configuration suggest that the vehicle is statically stable ( $\sim 0.45$  cal. of static margin).

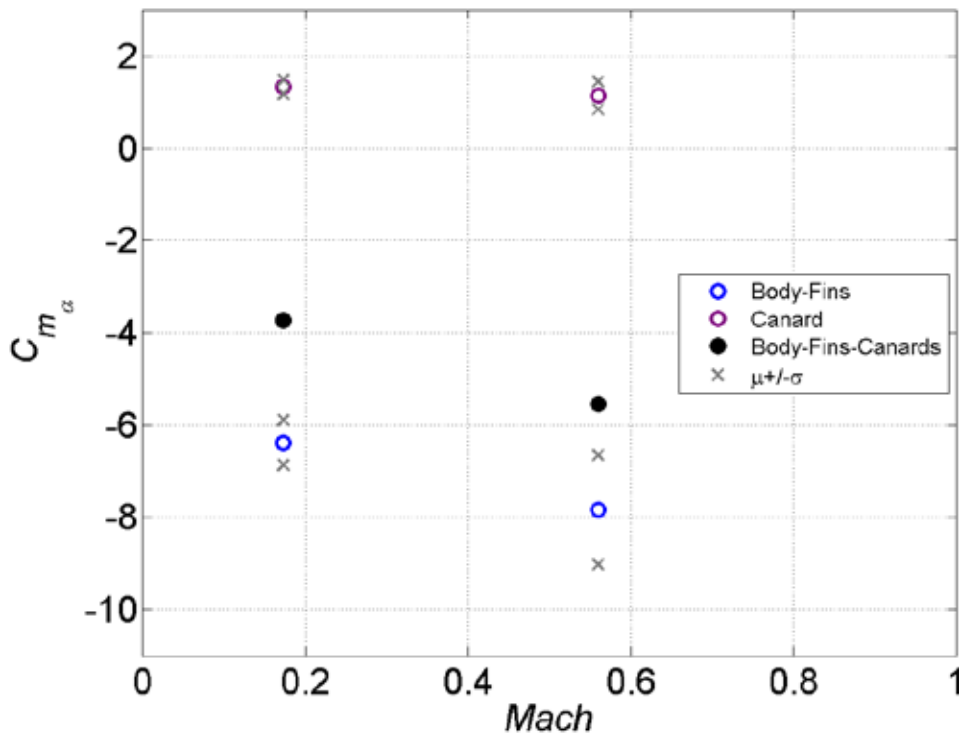


**Fig. 10 Summary linear in-plane static moment coefficients in dynamic wind tunnel**

Dynamic wind tunnel experiments were performed with the model constrained to the roll direction for investigation of the aerodynamic roll damping. The fins were canted to produce the roll motion and the angle of attack was  $0^\circ$ . The wind tunnel measurements and parameter estimation calculations using the aerodynamic model and rigid body dynamics is presented in Fig. 11. Results indicate low modeling error since the model matches the experiment to within  $0.63^\circ$  (root-sum-square error). This analysis yields the roll damping ( $C_{l_p} = -12.5$ ) and static roll moment ( $C_{l_0} = 0.0978$ ) coefficients.

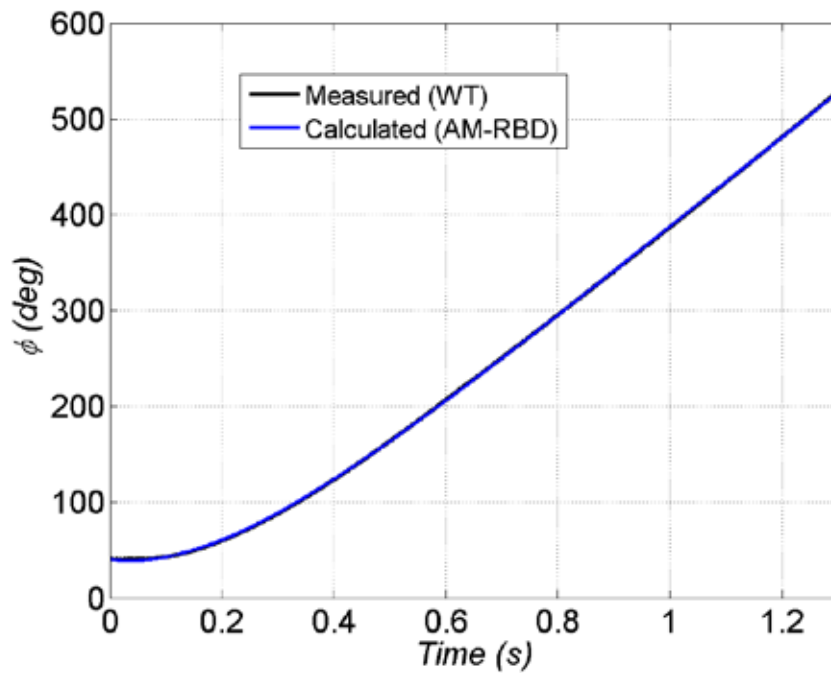


**Fig. 11 Free motion rolling in dynamic wind tunnel**

We now consider spark range experiments. Representative spark shadowgraphs are included in Fig. 12. These images were captured at the same instant in time in 2 orthogonal planes. The shadow cast by illuminating the vehicle onto the panel with the spark source is the black, in-focus shape and the blurred, lighter shape is the actual vehicle. The body, fins, canards, and roll pin are clearly visible and used to ultimately obtain the vehicle location and orientation.

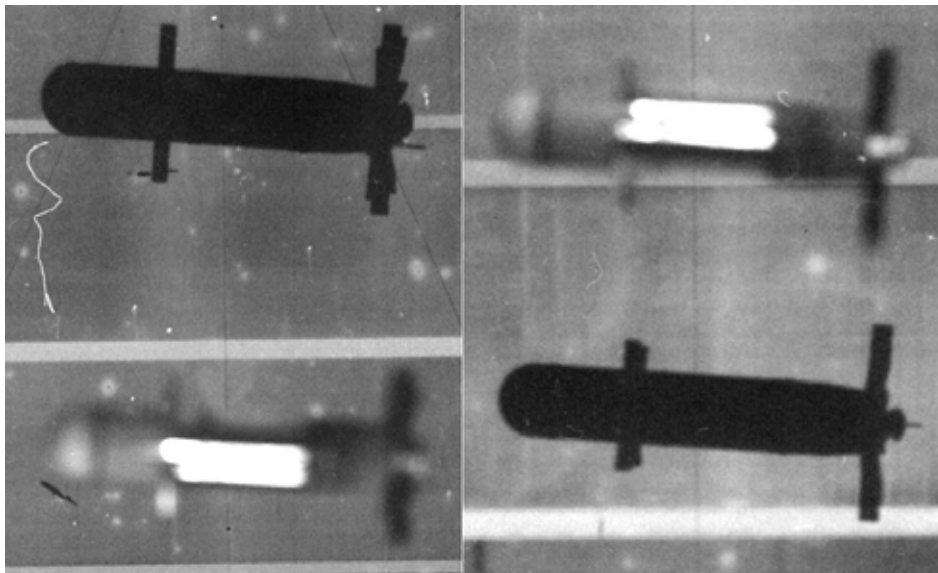


**Fig. 12 Spark shadowgraphs (left = vertical, right = horizontal)**

Typical flight motions in the spark range are given in Fig. 13. Points represent the measurements and the smooth curves represent the parameter estimation calculations. These data were for the body-fins-canards configuration with internal symmetry and canted fins. Recall that the gun was located within the enclosure slightly up-range of 50 m from the first measurement station. The upper-left plot illustrates that the vehicle rolls through about 6 revolutions prior to leaving the instrumentation at about 200 m. The pitching and yawing motion in the upper-right plot features a low amplitude ( $<2.5^\circ$ ) and is dominated by a trim that oscillates at the roll rate. This angular motion results in a helical motion in the center of gravity that is evident as the oscillations in the vertical and horizontal components in the bottom plot. The vertical component of center of gravity also bends due to the action of gravity. Overall, calculations matched experimental observations to within the measurement error, which validates the parameter estimation algorithm and indicates that the underlying aerodynamic model suitably captures the flight physics.

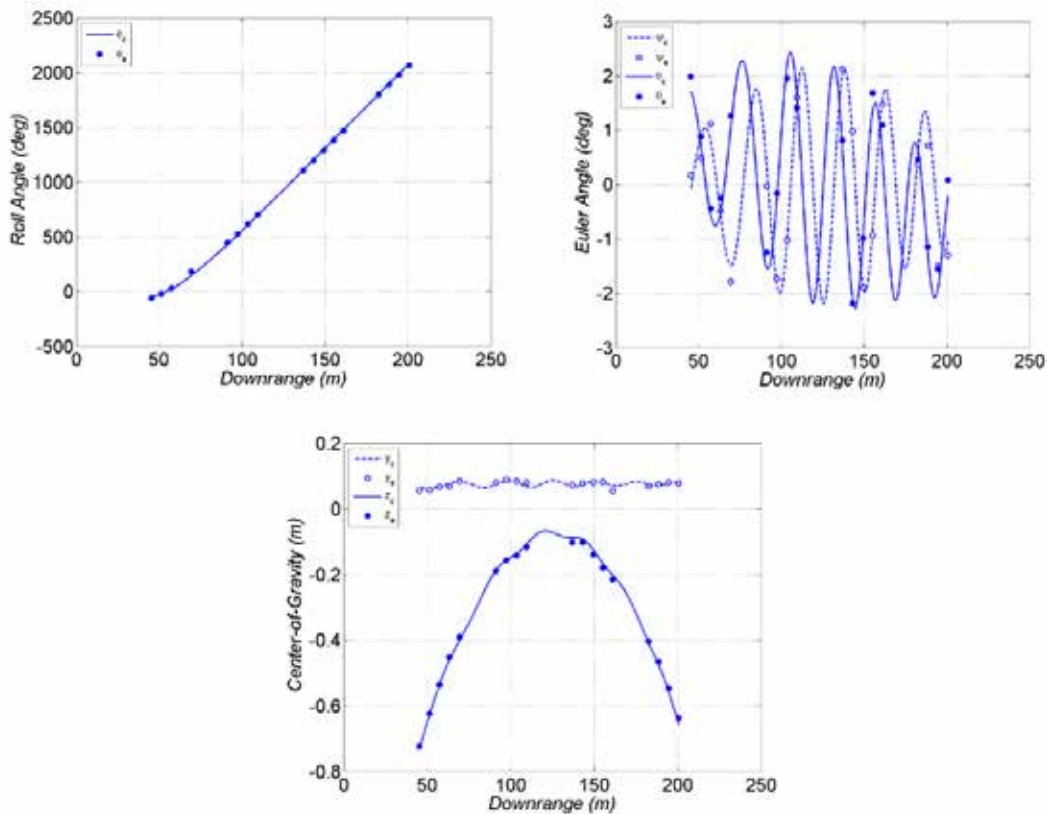


**Fig. 13 Flight motion in spark range (top left = roll, top right = pitch and yaw, bottom = center of gravity)**

Figure 14 explains the resonance behavior of this vehicle. The total angle of attack and roll rate calculated by the parameter estimation algorithm are plotted. The

vehicle natural frequency and trim amplification factor, detailed in Fresconi et al.<sup>26</sup> were also computed and plotted. These data indicate the vehicle is launched near zero roll rate and accelerates to about a 9-Hz roll rate within about 50 m from the gun. The vehicle natural frequency varies slightly with Mach number but stayed around 7 Hz during this flight. A resonance condition occurs as the roll rate and vehicle natural frequencies line up. The trim amplification factor increases near this condition indicating the potential for large total angle of attack. The total angle of attack increased after this resonance condition but the trim angle is small enough to keep total angle of attack below 2.5°. Internal mass asymmetries were emplaced within some vehicles to provide a higher trim angle when flying through resonance, which resulted in a higher total angle of attack.

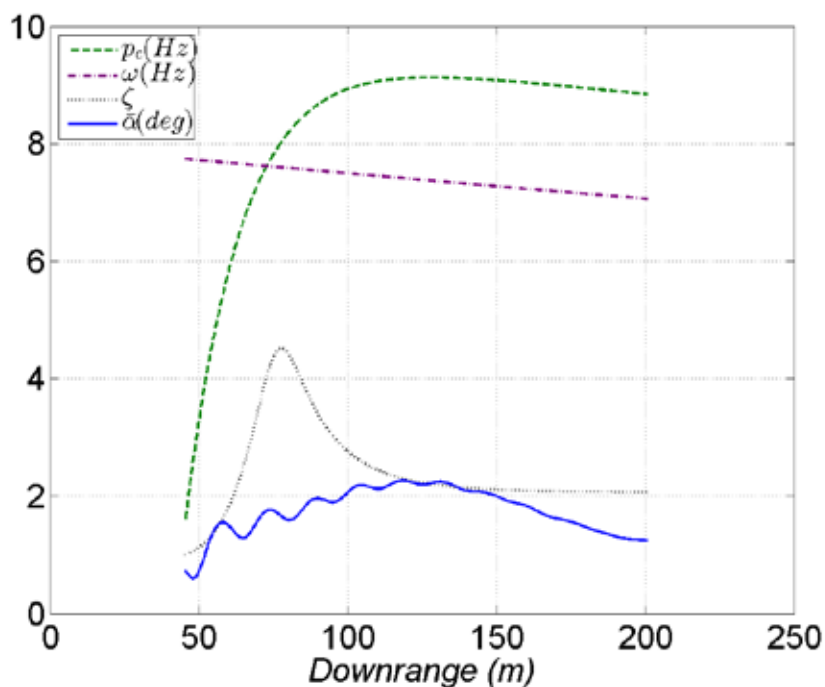


**Fig. 14 Resonance behavior of vehicle in spark range**

The total angle of attack histories from parameter estimation calculations for all spark range flights are collected in Fig. 15. Four of the flights remain below 3°. Two of these flights damp to below 1° because there was no fin cant and therefore no resonance. The other 2 flights below 3° feature a maximum angle of attack between 100 and 150 m downrange of the first measurement station due to the presence of fin cant and resonance. The final 2 flights also had fin cant and reached approximately 7° total angle of attack because an internal mass asymmetry ensured a higher trim angle was amplified during resonance. Achieving a range of angular motion is essential to accurately estimating aerodynamics (especially

nonlinearities). Different experimental vehicle flights were used to produce these desired angular motion spectra.

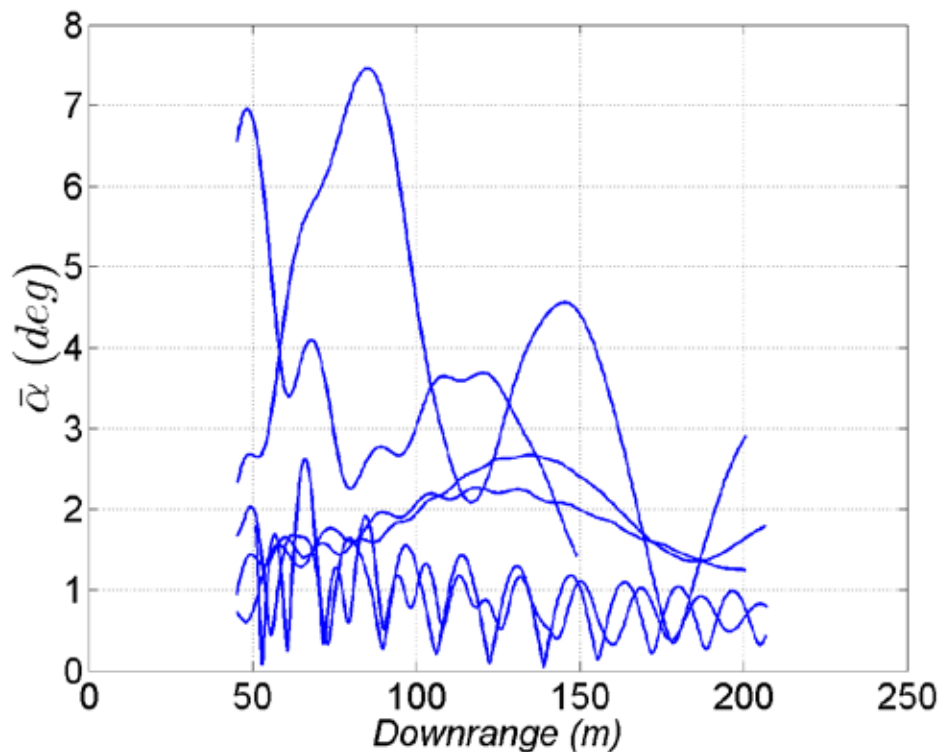


**Fig. 15 Total angle of attack for all spark range flights**

Aerodynamics from dynamic wind tunnel and spark range experiments are summarized next. Recall that the canard-fin-body configuration was studied for dynamic wind tunnel experiments and both canard-fin-body and fin-body models were flown during spark range experiments. In general, experiments consist of physical model variation (external shape), measurement errors, and practical effects which must be accounted for in the aerodynamic modeling (e.g., trims, static out-of-plane moments). The driving aerodynamic terms are the focus of this discussion.

Zero-yaw axial force coefficient variation with Mach number is presented in Fig. 16. The legend depicts the symbols used for dynamic wind tunnel and spark range experiments and identifies the vehicle configuration (fin-body and canard-fin-body). Inspection of these data shows that the canards add a small amount of additional zero-yaw axial force. The scatter in the spark range data is likely dictated by variation in the external shape. The wind tunnel zero-yaw axial force may be low due to sting effects. Wind tunnel data did not include collection of base pressure in an effort to correct for sting effects. The volume occupied by the sting near the

base of the vehicle would consist of complex vortical structures in the wake that increase drag for the vehicle in free-flight.

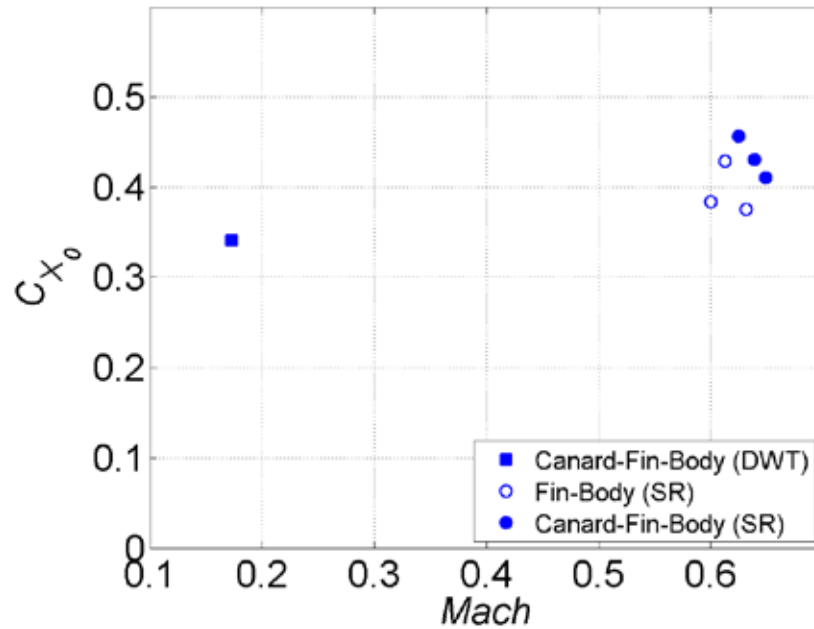


**Fig. 16 Zero-yaw axial force coefficient**

The linear normal force coefficient is provided in Fig. 17. Canards add appreciable normal force. Dynamic wind tunnel and spark range experiments agree favorably for normal force. Scatter in the spark range data is likely due to challenges in deducing normal force from swerving motion measurements.

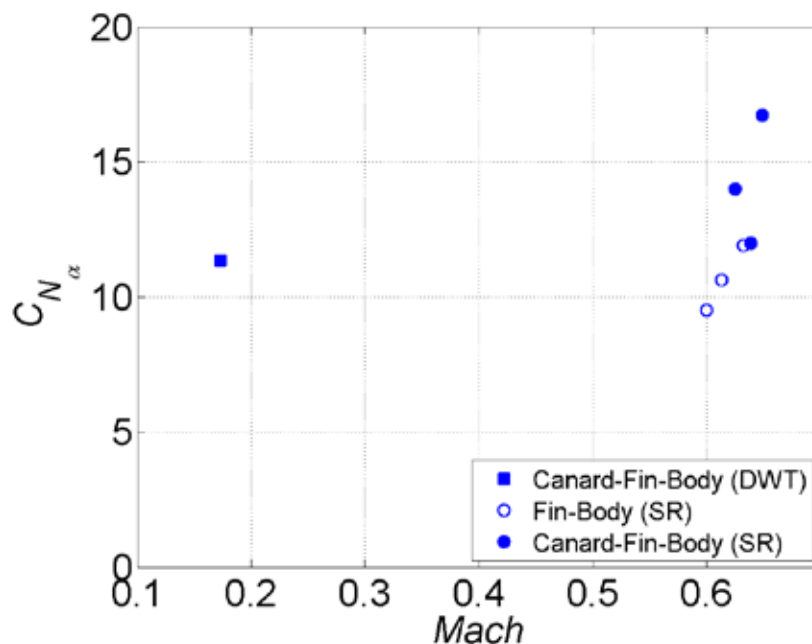


**Fig. 17 Linear normal force coefficient**

Linear in-plane static moment coefficients are given in Fig. 18. Canards significantly shift the aerodynamic center-of-pressure noseward. Overall agreement is good between dynamic wind tunnel and spark range results for the complete canard-fin-body configuration. The fin-body data is intrinsically different between dynamic wind tunnel and spark range techniques due to the nature of the experiments. The in-plane static moment for the fin-body was obtained from dynamic wind tunnel experiments with the canards mounted. This arrangement inherently includes the flow interactions described (i.e., induced downwash on fins from canards and subsequent reduction in pitch-yaw stability) in the aerodynamic modeling. The aerodynamic model includes the moments due to the fin-body alone, canard, and interaction of the canards with the fin-body. The fin-body in-plane static moment for the dynamic wind tunnel was obtained by subtracting the moments due to the canards and implicitly contains both the fin-body moment and the moment due to the interaction of the canards with the fin-body. The in-plane static moment for the fin-body was obtained from spark range experiments by firing vehicles without canards. For this situation, only the fin-body moment is present. Spark range fin-body linear in-plane static moment coefficient was more negative because the destabilizing effect of canard flow interactions were absent. Comparison of the canard-fin-body (both dynamic wind tunnel and spark range) with the fin-body (dynamic wind tunnel) and the fin-body (spark range) provides an estimate of the relative contributions of the moment due to the canards and the interaction effect of the canards with the fin-body. This result highlights the

importance of interactions in aerodynamic modeling approaches such as those proposed in Eqs. 5–6.

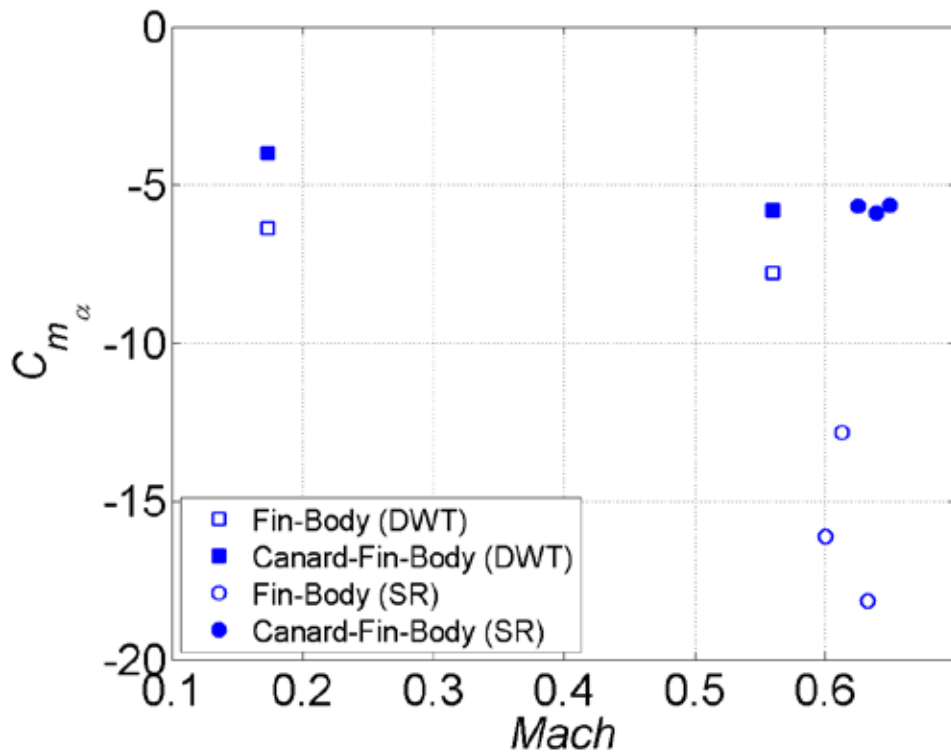


Fig. 18 Linear in-plane static moment coefficient

Aerodynamic damping coefficients are provided in Fig. 19. Canards moderately increase the damping. Results are consistent across the techniques and Mach numbers investigated.

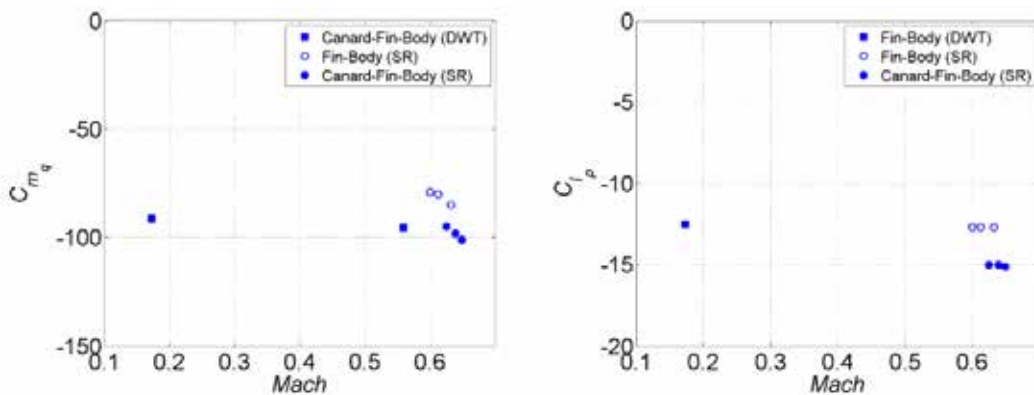


Fig. 19 Damping coefficients (left = pitch, right = roll)

## 7. Conclusions

---

This study was motivated by the need to improve knowledge of maneuvering flight for canard-controlled, subsonic missiles. This vehicle class experiences mechanisms such as separation and vortex interactions in this flight regime, which are only partially understood for canonical problems. These processes must be fully understood for more complex configurations to develop vehicle and control technology for enhanced kinematic capability.

The contributions of this study for maneuvering munitions fall within 3 areas: experimental techniques, experimental validation, and aerodynamic modeling. Dynamic wind tunnel experimental techniques were developed wherein the vehicle included onboard control actuation, processing, and sensing technologies to perform free motion, open- and closed-loop control maneuvers up to approximately Mach 0.7. The experimental setup accommodated full roll-pitch-yaw in addition to isolating roll and pitch motions. The model mounting limited intrusion while permitting up to approximately  $8^\circ$  total angle of attack. The instrumentation captured accurate angle of attack, canard deflection, and balance data. Free-flight experimental techniques were advanced by firing vehicles through the spark range with different configurations to isolate control (canard) aerodynamics. Resonance and internal mass asymmetries were used to produce a range of angular motion amplitudes, which is essential to accurately estimating aerodynamics.

These experimental techniques successfully provided static and dynamic aerodynamics up to  $8^\circ$  total angle of attack for use in validating computations. Aerodynamic coefficients compared favorably for dynamic wind tunnel and spark range experiments and were also consistent across Mach number. The zero-yaw axial force was likely low in dynamic wind tunnel experiments due to sting effects. The fin-body in-plane static moment was more negative in spark range firings due to the absence of canards and subsequent flow interactions.

Calculations of the flight motion matched the experimental data to within the measurement error indicating that parameter estimation algorithms were valid and the proposed aerodynamic models were appropriate. Flow separation on the canards was observed during dynamic wind tunnel experiments as a reduction in the aerodynamic effectiveness. Flow interaction effects typified by adverse roll control (i.e., reduction in control roll moment due to vortices shed off canards impinging on fins) and reduction in pitch-yaw stability (i.e., induced downwash on fins from canards) were encountered during experiments and successfully modeled with the approach outlined in Eqs. 4–6. Little evidence for coupling between roll and pitch-yaw was detected.

## 8. References

---

1. Rhie CM, Chow WL. Numerical study of the turbulent flow past an airfoil with trailing edge separation. *AIAA J.* 1983;21(11):1525–1532.
2. Ericsson LE, Reding JP. Steady and unsteady vortex-induced asymmetric loads on slender bodies. *JSPRO.* 1981;18(2):97–109.
3. Kiedaisch JW, Acharya M. Interaction of missile nose-tip vortices with a control surface. *AIAA J.* 1996; 34:999–1006.
4. Beresh SJ, Smith JA, Henfling JF, Grasser TW, Spillers RW. Interaction of a fin trailing vortex with a downstream control surface. *JSPRO.* 2009;46(2):318–328.
5. Beresh SJ, Henfling JF, Spillers RW. Planar velocimetry of a fin trailing vortex in subsonic compressible flow. *AIAA J.* 2009;47(7):1730–1740.
6. Pepitone TR, Jacobson ID. Resonant behavior of a symmetric missile having roll orientation-dependent aerodynamics. *JGCD.* 1978;1(5): 335–339.
7. Blair AB, Dillon JL, Watson CB. Experimental study of tail-span effects on a canard-controlled missile. *JSPRO.* 1993;30(5):635–640.
8. Meyer J. Effects of the roll angle on cruciform wind-body configurations at high incidences. *JSPRO.* 1994;31(1):113–122.
9. Maynes D, Gebert GA. High angle-of-attack aerodynamics of a missile geometry at low speed. *JSPRO.* 1999;36(5):772–774.
10. Burt JR. The effectiveness of canards for roll control. Redstone Arsenal (AL): Army Missile Command (US); 1976 Nov. Report No.: TR-RD-77-8.
11. Smith E, Hebbar SK, Platzer MF. Aerodynamic characteristics of a canard-controlled missile at high angles of attack. *JSPRO.* 1994;31(5):766–772.
12. Siltan SI, Coyle CJ. Effect of canard deflection on fin performance of a fin-stabilized projectile. 33rd AIAA Applied Aerodynamics Conference; 2015. AIAA; c2015. AIAA 2015-2586.
13. Siltan SI, Fresconi FE. Effect of canard interactions on aerodynamic performance of a fin-stabilized projectile. *JSPRO.* 2015;52(5):1430–1442.
14. Sahu J, Fresconi FE. Flight behaviors of a complex projectile using a coupled CFD-based simulation technique: open-loop control. 54th AIAA Aerospace Sciences Meeting; c2016. AIAA 2016-2025

15. Sahu J, Fresconi FE. Flight behaviors of a complex projectile using a coupled CFD-based simulation technique: closed-loop control. 34th AIAA Applied Aerodynamics Meeting; c2016. AIAA 2016-4332
16. Fresconi FE, Celmins I, Sifton SI, Costello MF. High maneuverability projectile flight using low cost components. *Aero Sci Tech*. 2015;41:175–188.
17. Sahu J, Fresconi FE. Aeromechanics and control of projectile roll using coupled simulation techniques. *JSPRO*. 2015;52(3):944–957.
18. Moore FG, Moore LY. Approximate method to calculate nonlinear rolling moment due to differential fin deflection. *JSPRO*. 2012;49(2):250–260.
19. Weinacht P. Projectile performance, stability, and free-flight motion prediction using computational fluid dynamics. *JSPRO*. 2004;41(2):257–263.
20. DeSpirito J, Sifton S, Weinacht P. Navier-Stokes predictions of dynamic stability derivatives: evaluation of steady-state methods. *JSPRO*. 2009;46(6):1142–1154.
21. Davison PM, Lowenberg MH, di Bernardo M. Experimental analysis and modeling of limit cycles in a dynamic wind-tunnel rig. *JAIR*. 2003;40(4):776–785.
22. Uselton BL, Uselton JC. Test mechanism for measuring pitch-damping derivatives of missile configurations at high angle of attack. Arnold Air Force Station (TN); Arnold Engineering Development Center (US); 1975. Report No.: AEDC-TR-75-43.
23. Fresconi FE, Celmins I, Ilg M, Maley J. Projectile roll dynamics and control with a low-cost skid-to-turn maneuver system. *JSPRO*. 2014;51(2):624–627.
24. Strub G, Dobre S, Gassmann V, Theodoulis S, Basset M. Pitch-axis identification for a guided projectile using a wind-tunnel-based experimental setup. *IEEE/ASME Trans Mecha*. 2016;21(3):1357–1365.
25. Whyte RH, Winchenbach GL, Hathaway WH. Subsonic free-flight data for a complex asymmetric missile. *JGCD*. 1981;4(1):59–65.
26. Fresconi FE, Guidos B, Celmins I, DeSpirito J, Hathaway W. Flight behavior of an asymmetric missile through advanced characterization techniques. *JSPRO*. 2017;54(1):266–277.
27. Nelson BP. Development and evaluation of a dynamic, 3-degree-of-freedom (DOF) wind tunnel model. Army Research Laboratory (US); Nov 2016. Report No.:ARL-CR-0807.

28. Schmidt EM, Donovan WF. Technique to reduce yaw and jump in fins-stabilized projectiles. JSPRO. 1998;35(1):110–111.
29. Chapman GT, Kirk DB. A method for extracting aerodynamics coefficients from free-flight data. AIAA J. 1971;8(4):753–758.
30. Illiff K. Parameter estimation for flight vehicles. JGCD. 1989;12(5)609–622.
31. Klein V, Morelli EA. Aircraft system identification. AIAA Education Series. Reston (VA): AIAA; 2006. p. 181–221.

## List of Symbols, Abbreviations, and Acronyms

---

2-D 2-dimensional

3-D 3-dimensional

ARL US Army Research Laboratory

CFD computational fluid dynamics

DSP digital signal processor

ECBC Edgewood Chemical Biological Center

1 DEFENSE TECHNICAL  
(PDF) INFORMATION CTR  
DTIC OCA

2 DIRECTOR  
(PDF) US ARMY RSRCH LAB  
RDRL CIO L  
IMAL HRA MAIL & RECORDS  
MGMT

1 GOVT PRINTG OFC  
(PDF) A MALHOTRA

46 DIR USARL  
(PDF) RDRL WM  
J S ZABINSKI  
RDRLWML  
P J PEREGINO  
RDRL WML A  
WF OBERLE III  
L STROHM  
RDRL WML B  
N J TRIVEDI  
RDRL WML C  
S A AUBERT  
RDRL WML D  
R A BEYER  
A BRANT  
J COLBURN  
P CONROY  
M NUSCA  
Z WINGARD  
RDRL WML E  
P WEINACHT  
V A BHAGWANDIN  
I CELMINS  
J DESPIRITO  
L D FAIRFAX  
F E FRESCONI III  
J M GARNER  
G S OBERLIN  
T PUCKETT  
J SAHU  
S I SILTON  
RDRL WML F  
M ILG  
B ALLIK  
G BROWN  
E BUKOWSKI  
B S DAVIS  
M DON  
D EVERSON  
M HAMAOU  
B KLINE  
J MALEY  
C MILLER

P MULLER  
B NELSON  
B TOPPER  
RDRL WML G  
J T SOUTH  
W DRYSDALE  
M MINNICINO  
RDRL WML H  
J F NEWILL  
T EHLERS  
E KENNEDY  
R SUMMERS  
C MEYER  
RDRL WMP  
D H LYON

2 ARO  
(PDF) S STANTON  
M MUNSON

2 VTD  
(PDF) C KRONINGER  
B GLAZ

9 RDECOM AMRDEC  
(PDF) L AUMAN  
J DOYLE  
S DUNBAR  
R MATHUR  
V OVERSTREET  
B GRANTHAM  
M MCDANIEL  
B MCINTOSH  
C ROSEMA

1 RDECOM ECBC  
(PDF) D WEBER

26 RDECOM ARDEC  
(PDF) D CARLUCCI  
J CHEUNG  
S K CHUNG  
D L CLER  
B DEFRANCO  
M DUCA  
P FERLAZZO  
R FULLERTON  
R GORMAN  
J C GRAU  
M HOHIL  
M HOLLIS  
R HOOKE  
M KOENIG  
A LICHTENBERG SCANLAN  
E LOGSDON  
M LUCIANO

	P MAGNOTTI G MALEJKO M PALATHINGAL J ROMANO T RECCHIA C STOUT W TOLEDO E VAZQUEZ C WILSON	1 (PDF)	GTRI A LOVAS
2 (PDF)	PEO AMMO C GRASSANO P MANZ	2 (PDF)	ISL S THEODOULIS P WERNERT
2 (PDF)	PM CAS P BURKE M BURKE	3 (PDF)	DRDC D CORRIVEAU C A RABBATH E GAGNON
1 (PDF)	MCOE A WRIGHT	4 (PDF)	DSTL M HILL T BIRCH
3 (PDF)	ONR P CONOLLY D SIMONS R SULLIVAN	1 (PDF)	DSTO N DUONG
4 (PDF)	NSWCDD L STEELMAN K PAMADI MALIN J FRAYSSE	2 (PDF)	GEORGIA INST OF TECH M COSTELLO J ROGERS
2 (PDF)	NAWCWD R SCHULTZ M MURPHREE	1 (PDF)	ROSE HULMAN INST OF TECH B BURCHETT
4 (PDF)	AFRL T J KLAUSUTIS R MURPHEY C PASILIAO S TEEL	1 (PDF)	UNIV OF SOUTH FLORIDA T YUCELEN
1 (PDF)	AFOSR EOARD G ABATE	1 (PDF)	ARROW TECH W HATHAWAY
1 (PDF)	MARCORSYSCOM P FREEMYERS	6 (PDF)	ATK R DOHRN M HEIBEL S OWENS W JENSEN S UZPEN M WILSON
1 (PDF)	DARPA J DUNN	4 (PDF)	BAE B GOODELL P JANKE O QUORTRUP D JUNGQUIST
1 (PDF)	NASA I GREGORY	1 (PDF)	GD OTS D DEDMONDS
1 (PDF)	DRAPER LAB G THOREN	2 (PDF)	UTAS P FRANZ S ROUEN

2 LMMFC  
(PDF) G KANGA  
D PICKEREL

2 RMS  
(PDF) D STRASSMAN  
S WITHERSPOON

1 STA  
(PDF) D MAURIZI